



Nanoscale

Thick grain boundary induced strengthening in nanocrystalline Ni alloy

Journal:	<i>Nanoscale</i>
Manuscript ID	NR-ART-08-2019-006843.R1
Article Type:	Paper
Date Submitted by the Author:	24-Oct-2019
Complete List of Authors:	<p>Ding, Jie; Purdue University System, School of Materials Engineering Neffati, Dajla; University of Houston, Department of Mechanical Engineering Li, Qiang; Purdue University , Materials engineering Su, Ruizhe; Purdue University, Materials Engineering Li, Jin; Purdue University, School of Materials Engineering Xue, Sichuang; Purdue University Shang, Zhongxia; Purdue University, School of Materials Engineering Zhang, Yifan; Purdue univarsity, School of Materials Engineering Wang, Haiyan; Purdue University System, School of Materials Engineering; Purdue University, School of Electrical and Computer Engineering Kulkarni, Yashashree; University of Houston, Department of Mechanical Engineering Zhang, Xinghang; Purdue University System, Materials Engineering</p>

SCHOLARONE™
Manuscripts

Thick grain boundary induced strengthening in nanocrystalline Ni alloy

Jie Ding^a, D. Neffati^b, Q. Li^a, R. Su^a, Jin Li^a, S. Xue^a, Z. Shang^a, Y. Zhang^a, H. Wang^{a,c}, Y. Kulkarni^b, and X. Zhang^{a,*}

^a School of Materials Engineering, Purdue University, West Lafayette, IN 47907, USA

^b Department of Mechanical Engineering, University of Houston, Houston, TX 77204, USA

^c School of Electrical and Computer Engineering, Purdue University, West Lafayette, IN 47907, USA

Corresponding author: X. Zhang; xzhang98@purdue.edu

Abstract

Grain refinement has been extensively used to strengthen metallic materials for decades. Grain boundaries act as effective barriers to the transmission of dislocations and consequently lead to strengthening. Conventional grain boundaries have a thickness of 1-2 atomic layers, typically ~0.5 nm for most metallic materials. Here we report, however, the formation of ~3 nm thick grain boundaries in nanocrystalline Ni alloy. *In-situ* micropillar compression studies coupled with molecular dynamics simulations suggest that the thick grain boundaries are stronger barriers than conventional grain boundaries to the transmission of dislocations. This study provides a fresh perspective for the design of high strength, deformable nanostructured metallic materials.

Key words: Thick grain boundaries, Strengthening, Nanocrystalline metals, In situ compression, MD simulation

1. Introduction

The contribution of grain boundaries (GBs) to the strength of polycrystalline metals has been intensively investigated since the beginning of 1950s, when Hall and Petch reported the dependence of strength on grain size of metallic materials by using the Hall-Petch equation ¹:

$$\sigma_y = \sigma_0 + kd^{-1/2} \quad (1),$$

where σ_y is yield strength, σ_0 is friction stress, k is a coefficient describing the barrier resistance of GBs to slip transmission of dislocations, and d is the average grain size ¹⁻³. The grain size dependent strengthening mechanisms have been studied extensively for various types of boundaries or interfaces in nanostructured metallic materials fabricated by plastic deformation ^{2,4-6}, electrodeposition ⁷ and magnetron sputtering ¹⁰⁻¹⁷.

As predicted by the Hall-Petch equation, the strengthening effect becomes more prominent with a higher k value. The coefficient k characterizes the intrinsic resistance of GBs to the slip transmission of dislocations. It has been proven that the character and structure of GBs play an important role in impeding dislocation slip in metallic materials ¹⁸. Sangid *et al* ¹⁸ studied the effect of energy barrier to dislocation transmission through GBs and dislocation nucleation from GBs, and showed that the coherent ($\Sigma 3$) twin boundary is a stronger barrier to the transmission of dislocations than other types of GBs, such as the $\Sigma 13$ and $\Sigma 19$ GBs. Koning *et al* ¹⁹ also found that the slip transmission resistance of GB is determined by three variables: the ratio of resolved stress on the incoming slip system to that on the outgoing slip system, the magnitude of any residual Burgers vector content left in the GB, and the angle between the traces of the incoming and outgoing slip planes. Several other mechanisms on interfaces induced strengthening, including modulus and lattice parameter mismatch ^{12,14,20,21}, interfacial shear strength ²⁰⁻²³, have

also been discussed. Prior study also showed that nitrogen increases the k value of austenitic steel (Cr18Ni16Mn10) significantly by blocking dislocation source in grains²⁴. Hu *et al*⁸ reported that annealing of the electrodeposited nanocrystalline (NC) NiMo alloy led to high hardness, 11.0 GPa, due to the segregation of Mo nanoclusters to GBs.

GB segregation and the formation of GB complexions, have been investigated previously²⁵⁻³⁴. GB complexion was first reported in ceramic systems³⁵, and has since also been observed in metallic materials. For instance, the segregation of Ga in Al GBs is believed to play an important role in embrittlement due to the formation of GB complexion²⁵. Similar phenomena have also been observed in Cu-Bi²⁹, Ni-Mo²⁷ and W-Ni²⁶ systems. While for the Zr doped nanograin Cu powders, the mechanical tests showed a yield strength exceeding 1 GPa and a strain to failure of more than 50%, which is rare in traditional Cu alloys³⁴. The combination of high strength and good ductility of the Cu-Zr powder is attributed to the formation of amorphous intergranular films in the Cu GBs, as the amorphous intergranular films can increase the GB tolerance to the transmission of dislocations by absorbing dislocations and acting as an effective defect sinks^{32,34}.

Most previous studies focus on the strengthening effect of GBs with thickness of 1-2 atomic layers, ~0.5 nm. The influences of thick GBs or GB complexions on the mechanical properties of metallic materials, especially for bulk metallic materials, are largely unclear. In this study, we reported the formation of thick GBs, with an average thickness of ~3 nm, in nanocrystalline (NC) Ni alloy fabricated by severe plastic deformation. The thick GBs formed by Mo segregation to the GBs during heat treatment. *In-situ* micropillar compression tests show that thick GBs induced much more pronounced strengthening effect than conventional GBs.

Molecular dynamics (MD) simulations provide atomistic insights into the underlying strengthening mechanism of thick GBs.

2. Experimental methods

2.1 Materials and processing.

A Hastelloy C-22HS Ni alloy rod (12 mm in diameter), with a chemical composition (in Wt.%) of Cr 21.0, Mo 17.0, Fe 2.0, C 0.01, Si 0.08, balanced by Ni, was subjected to SMGT at room temperature. Prior to processing, the C-22HS alloy was annealed at 1100 °C for 1 hr, followed by air cooling. Details on the SMGT technique can be found elsewhere³⁶. During processing, the rod rotated at a speed of 400 rpm, while a hemispherical WC/Co tool tip penetrated into sample surface by 30 μm and slid along axial direction at a velocity of 10 mm/min. The process was repeated 8 times to generate subsequent deformation zones underneath the surface. Heat treatment of the processed alloys was carried out at 650 °C for 5 hr in a tube furnace.

2.2 Microstructure characterization.

The microstructure and composition analysis of the specimens were carried out on an FEI Talos 200X analytical transmission electron microscope operated at 200 kV, equipped with a super X energy-dispersive X-ray spectroscopy (EDS) detector. TEM specimens were prepared by focused ion beam (FIB) technique using an FEI Quanta 3D FEG Dual beam FIB scanning electron microscope following typical protocols.

2.3 *In-situ* micropillar compression tests

Micropillars were prepared using FIB technique along the longitudinal direction of both as-processed and heat-treated C-22HS alloy in the NC layer. The micropillars have a diameter of $\sim 2 \mu\text{m}$ and height of $\sim 5 \mu\text{m}$ with a height-to-diameter aspect ratio of ~ 2.5 to avoid buckling during compression tests. *In-situ* microcompression tests at a constant strain rate of $1 \times 10^{-3} \text{s}^{-1}$ were performed in an FEI Quanta 3D FEG SEM microscope using a Brukers-Hysitron PI 88×R PicoIndenter equipped with a $5 \mu\text{m}$ diameter diamond flat-punch indenter tip. The force-displacement data were collected by the piezoelectric actuator in the capacitive transducer. The morphological evolution of the micropillar during compression was recorded by SEM video. All micropillars were compressed under displacement control mode until $\sim 18\%$ of strain, followed by 0.5 s holding before unloading. The drift rate was measured to be 0.1 nm/s.

Pillar diameters, measured at the half-height of the pillar, were used for the calculation of engineering stress. The engineering stress calculated in this study represents an approximation considering the small taper angle of pillars, $< 3^\circ$. To obtain an accurate measurement of strain, the equation derived by Sneddon³⁷ was applied to calculate displacement, x ,

$$x = x_{meas} - \frac{1 - \nu_i^2}{E_i} \left(\frac{F_{meas}}{D_t} \right) - \frac{1 - \nu_b^2}{E_b} \left(\frac{F_{meas}}{D_b} \right) \quad (2),$$

where x_{meas} and F_{meas} represent the measured displacement and force, respectively. ν_i and E_i are the Poisson's ratio and Young's modulus of diamond punch, taken to be 0.07 and 1220 GPa, respectively. ν_b and E_b for Ni are 0.31 and 205 GPa, respectively. D_t and D_b are the diameter of the pillar near the top and bottom portion, respectively. The engineering stress-strain curves were obtained after the correction of displacement, and subsequently converted to true stress-strain curves by using the homogeneous deformation model (assume no volume change during the deformation).

2.4 MD simulation details

MD simulations were performed on two different sets of NiMo bilayers with pre-existing GBs using the Large-scale Atomic/Molecular Massively Parallel Simulator (LAMMPS)³⁸ and the results were visualized using Ovito³⁹ and DXA⁴⁰. The bilayers are $11 \text{ nm} \times 11 \text{ nm} \times 10.5 \text{ nm}$ and are periodic in the z-direction. The GBs separate two grains of equal thicknesses in the y-direction. The first simulation is intended to study the effect of a regular $\Sigma 5$ GB on dislocation nucleation and motion. To investigate the effect of a thick GB, we take a sample with a similar setup as the one previously described and create an amorphous boundary separating the two grains following the steps in Ref.⁴¹. First, the atoms are held rigid except for a 1.5 nm slab around the GB that is melted to 1600K and held for 200 ps. Then, the melted atoms are quenched from 1600K to 800K over 200 ps. Later, to relax the system, the fixed atom constraint is removed and the entire sample is quenched from 800 to 300K over 40 ps. Finally, the sample is relaxed at 300K under the NVT ensemble with a Nose-Hoover thermostat for an additional 20 ps, resulting in a bilayer with a thick amorphous boundary of $\sim 2.5 \text{ nm}$. In both samples, a thin layer of 10 nm in thickness and 5.5 nm in width is removed to create a step that acts as a dislocation nucleation site. Eventually, both structures undergo equilibration at 300K for 50 ps under the same ensemble previously used. Tension is applied for 600 ps in the x-direction at a strain rate of 10^8 s^{-1} . The Ni-Mo, Ni-Ni and Mo-Mo atomic interactions are described by the embedded-atom method (EAM) potential developed by Zhou *et al*⁴².

3. Results

3.1 Microstructure characterization

The microstructure of the as-processed sample in Fig.1 reveals that NC grains, as verified by the inserted selected area diffraction (SAD) pattern, have formed after SMGT (Fig.1a1). The average grain size is ~ 37 nm at ~ 8 μm from treated surface. The scanning transmission electron microscopy (STEM) image and corresponding EDS maps in Fig.1a2 show that the major chemical elements (Ni, Mo, Cr) are distributed uniformly in the as-processed specimen. High resolution TEM (HRTEM) image in Fig.1a3 shows deformation twins (DTs), several nanometers in thickness, and stacking faults (SFs) inside grains. The GBs (as labeled by white dotted lines) are sharp and narrow. However, after heat treatment at 650 °C for 5 hr, the average grain size of NC grains at the same depth coarsened to ~ 53 nm (Fig.1b1). A comparison of grain size distribution of as-processed and heat-treated samples at depth of ~ 8 μm is shown in Suppl.Fig.1. The EDS maps in Fig.1b2 show the enrichment of Mo along GBs, accompanied by the depletion of Ni in the heat-treated Ni alloy. An EDS map at lower magnification including multiple grains in Suppl.Fig.2a shows that most GBs in the heat-treated specimen are enriched in Mo. The corresponding compositional line profile across a typical GB in Suppl.Fig.2c (as marked by the dash line in STEM image in Suppl.Fig.2b) also verifies the Mo-enrichment of GBs, and the thickness of Mo-rich zone is several nanometers. The HRTEM image in Fig.1b3 reveals that the thickness of Mo rich GBs is ~ 3 nm, which is much thicker than those in the as-processed alloy, ~ 0.5 nm. The distribution of GB thickness for the heat-treated specimen is shown in Suppl.Fig.3. The atomic arrangement within the thick GB region is disordered, as indicated by the yellow dashed circles. The corresponding fast Fourier Transform (FFT) of the image exhibits a combination of diffraction spots and amorphous ring, indicating the coexistence of crystalline and disordered structure within the thick GB region.

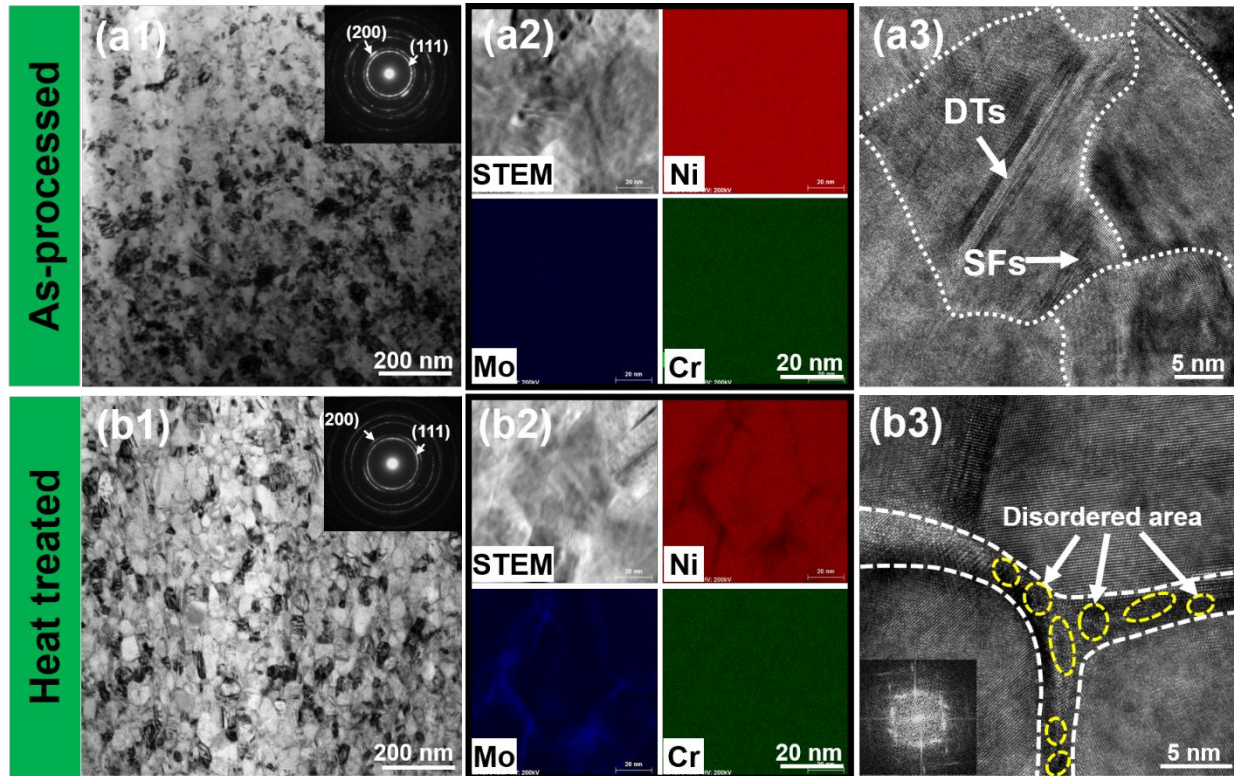


Figure 1. Comparison of the microstructures of the nanocrystalline surface layers of (a) as-processed and (b) 650°C/5h heat-treated C-22HS specimens. (a1, b1) TEM images showing nanocrystalline grains of specimens before and after heat treatment. (a2, b2) The STEM images and corresponding EDS maps showing the uniform distribution of major chemical elements (Ni, Mo, Cr) in as-processed specimen vs Mo enrichment in the GBs of the heat-treated specimen. (a3, b3) HRTEM images showing DTs and SFs inside grains of the as-processed specimen, and the thick Mo enriched GBs in the heat-treated specimen.

3.2 Mechanical properties

In-situ micropillar compression tests were performed in the NC layer of both as-processed and heat-treated specimens. The true stress-strain curves in Fig.2a1 and 2b1 show that

the flow stress of as-processed specimen with thin GBs (refers to thin GB sample hereafter) is ~ 1.8 GPa, whereas the flow stress of heat-treated specimen with thick GB (refers to thick GB sample hereafter) increases to ~ 2.4 GPa. Multiple micropillar compression tests were performed and the results are reproducible. The SEM snapshots of the video captured during compression of the thin GB specimens in Fig.2(a2-a6) show the uniform deformation of pillar as evidenced by classical barreling near the top of the deformed pillar. The corresponding pillar morphology evolution of the thick GB specimen in Fig.2(b2-b6) reveals similar uniform deformation behavior up to the compression strain of $\sim 20\%$. See supplementary video 1 and 2 for details.

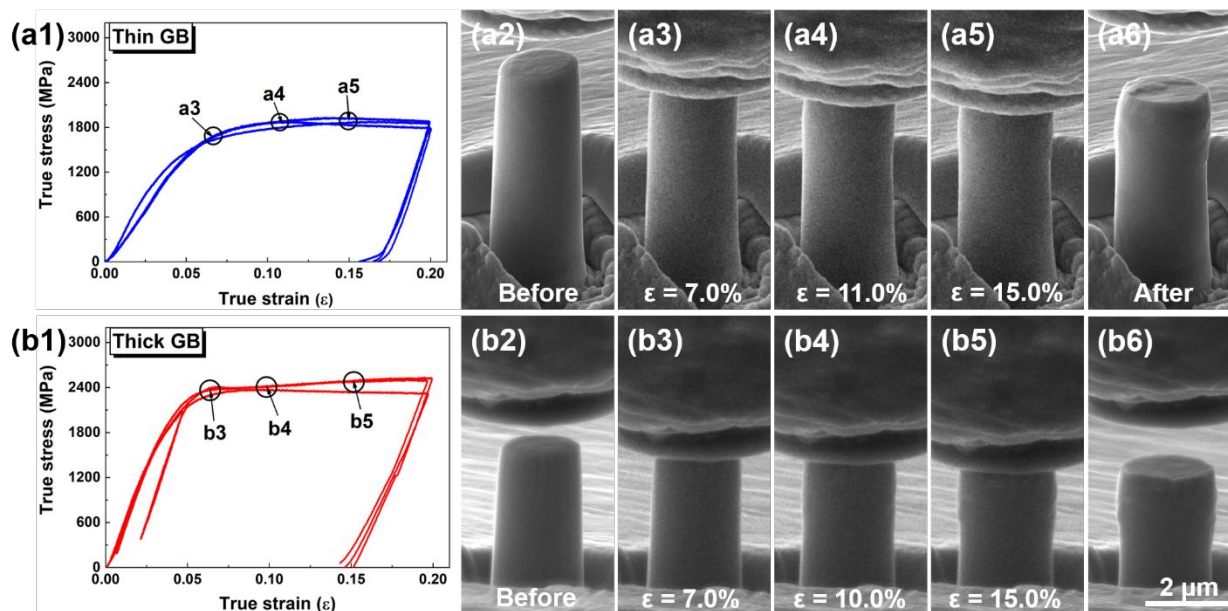


Figure 2. *In-situ* compression test results of pillars obtained from thin GB and thick GB specimens. (a1 and b1) The true stress-strain curves of thin GB and thick GB specimens. (a2-a6 and b2-b6) Corresponding SEM images of the specimens showing the pillar morphology evolution during compression tests. (See supplementary video 1 and 2 for details).

3.3 Hall-Petch relationship

Gradient structure with increasing grain size along the depth direction is produced after SMGT. To reveal the relationship of grain size and mechanical properties of both thin GB and thick GB specimens, the statistical studies of grain size along the depth direction were performed, and the corresponding Vickers hardness evolution was investigated. Fig.3a shows the evolution of grain size and Vickers hardness of the thin GB and thick GB specimens. The grain size of thin GB sample was ~ 33 nm at the depth of ~ 4 μm under the treated surface, then increased to ~ 104 nm at the depth of ~ 30 μm . Meanwhile, the hardness of the corresponding region decreased from ~ 5.8 GPa from the surface layer to ~ 4.3 GPa at the depth of ~ 40 μm from surface. After heat treatment at 650 $^{\circ}\text{C}$ for 5 hr, the average grain size coarsened slightly, from ~ 42 nm near the surface to ~ 120 nm at a depth of ~ 30 μm from surface. However, the Vickers hardness of thick GB sample is much higher than that of the thin GB one. The Vickers hardness on the topmost layer is ~ 7.7 GPa, then decreased to ~ 5.6 GPa at the depth of ~ 40 μm . Fig.3b shows the comparison of the Hall-Petch plot of the thin GB and thick GB specimens in this work with those data on NC Ni⁴³⁻⁵¹. It reveals that the thin GB sample has similar Hall-Petch slope (as shown by the red dash line) compared to the published data. While the hardness of the thick GB specimens is much higher than the thin GB specimen with similar grain size, and thus resulting in a greater Hall-Petch slope (red solid line) than other Ni alloys in Fig. 3b.

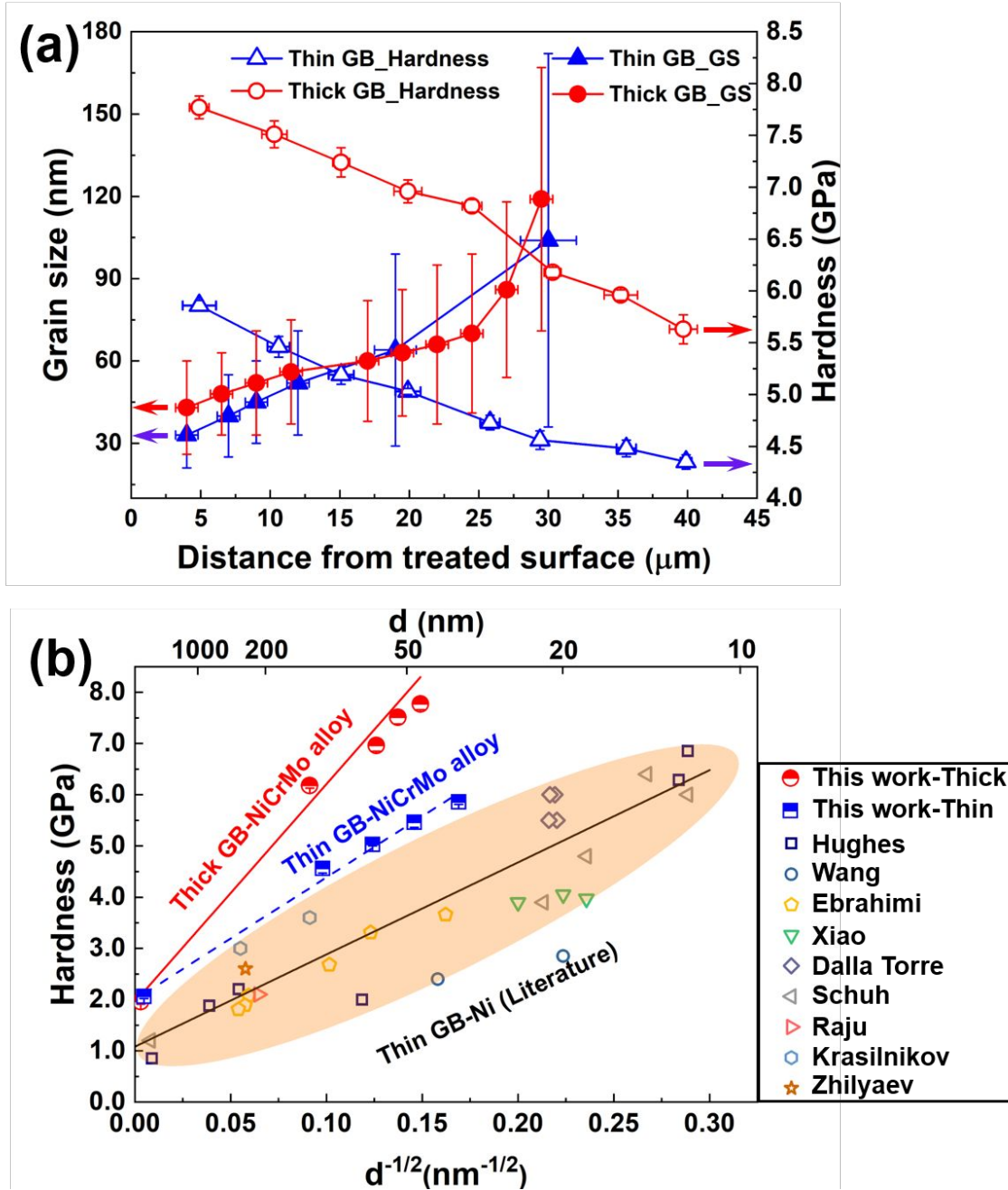


Figure 3. (a) The evolution of average grain size and Vickers hardness of thin GB and thick GB samples along the depth direction. (b) Comparison of the Hall-Petch plot from this study to published work on NC Ni⁴³⁻⁵¹.

4. Discussion

4.1 The formation of Mo-rich thick GB

The GB segregation and the formation of GB complexion have been studied extensively. The GB segregation phenomena have been reported in several binary systems, such as Cu-Zr^{34,52}, Cu-Nb⁵²⁻⁵⁴, Cu-Bi²⁹, Cu-Fe^{53,54}, Cu-Ag⁵⁴, Ni-Zr⁵², Ni-Mo²⁷, W-Ni²⁶, and alloys such as Fe-Mn-C steels⁵⁵. Six types of complexions have been classified by Dillion *et al*⁵⁶ according to their thickness, ordering and composition, while the disordered versions can be further classified as amorphous intergranular films (AIFs). The Mo-rich thick GB with disordered atomic structures observed in this study may also be similar to AIFs to some extent. Prior studies suggest that the formation of GB complexions is controlled by the enthalpy of segregation (ΔH_{seg}), enthalpy of mixing (ΔH_{mix}) and atomic radius mismatch⁵². ΔH_{seg} and ΔH_{mix} are the primary factors determining the type of complexions, and the atomic radius mismatch determines the stability of AIFs⁵². A positive ΔH_{seg} coupled with a negative ΔH_{mix} may promote the formation of AIF in alloys⁵². In this study, the Ni-Mo binary system possesses positive ΔH_{seg} and negative ΔH_{mix} ⁵⁷, a nanoscale AIF with disordered atomic structures along the GBs is therefore expected to form after heat treatment, consistent with the experimental observations.

4.2 Experimental evidence of thick GB induced strengthening

The microstructure characterizations show that the heat treatment induced grain coarsening by over 30% within 10-15 micron near surface (Fig.3a). However, the *in-situ* micropillar compression tests reveal that the flow stress of pillars increased from 1.8 GPa for the thin GB sample to 2.4 GPa for the thick GB one, consistent with the Vickers hardness

measurement at similar depth. The strengthening effect accompanied with the grain coarsening is surprising as conventional wisdom suggests that smaller grains often lead more pronounced strengthening⁵¹. Meanwhile other widely discussed conventional strengthening mechanisms arising from higher density defect or precipitates⁵⁸⁻⁶⁶, solute atoms^{67,68} are also absent in this case. These observations imply that the thick Mo enriched GB may play a critical role in annealing induced strengthening in NiCrMo alloy.

Hall-Petch mechanism typically dominates the grain size dependent strengthening of metallic materials when grain size is larger than 30 nm¹⁹⁻²¹. The Hall-Petch slope k is a measure of the GB resistance to slip transmission of dislocation and can be described by⁶⁹:

$$k = \sqrt{\frac{\tau^* \mu b}{\pi(1-\nu)}} \quad (3),$$

where τ^* is the critical shear stress required for slip transmission of dislocation across boundaries and is an indication of boundary barrier strength, μ is the shear modulus, b is the magnitude of Burgers vector and ν is the Poisson's ratio. The measured Hall-Petch slope for Vickers hardness plot k_{Hardness} can be converted to k by considering a Taylor factor of 3.1 and a hardness-to-flow stress conversion factor of 2.7 ($k = k_{\text{Hardness}}/3.1/2.7$)^{27,28}. The measured Hall-Petch slope for the thin GB and thick GB samples is 23.87 GPa $\sqrt{\text{nm}}$ and 42.54 GPa $\sqrt{\text{nm}}$, respectively. Thus, we obtain $k_{\text{thin}} = 2.85$ GPa $\sqrt{\text{nm}}$ and $k_{\text{thick}} = 5.08$ GPa $\sqrt{\text{nm}}$ for the thin GB and thick GB specimens. By using $\mu = 80$ GPa, $b = 0.248$ nm and $\nu = 0.30$ for Ni alloy, the boundary barrier strengths of thin GB and thick GB samples are calculated to be $\tau_{\text{thin}}^* = 0.90$ GPa and $\tau_{\text{thick}}^* = 2.86$ GPa, respectively. These analyses suggest that the thick GB is a much stronger barrier to the transmission of dislocations than the conventional GB of the thin GB Ni alloys.

To investigate the response of thick GBs to deformation, post compression TEM analyses were performed on the deformed pillars of thick GB specimen (36% of compression strain). The bright field and dark field TEM images in Fig.4a and b show that there is an insignificant grain size variation in the deformed pillar. HRTEM image showing the interior of grains in the deformed region (Fig.4c) reveals high-density SFs generated during compression (indicated by orange arrows), as verified by the corresponding FFT pattern in Fig.4d. The FFT patterns of the grains on the left and right side of thick GB in Fig.4c reveal that there was only a $\sim 5^\circ$ tilting between the (111) planes of these two grains. Interestingly, these SFs in the left grain were mostly blocked by the ~ 3 nm thick GB (labeled by double white dash lines). HRTEM image in Fig.4e (the magnified box e from Fig.4c) shows the SFs (indicated by white arrows) were not able to transmit across the thick GB.

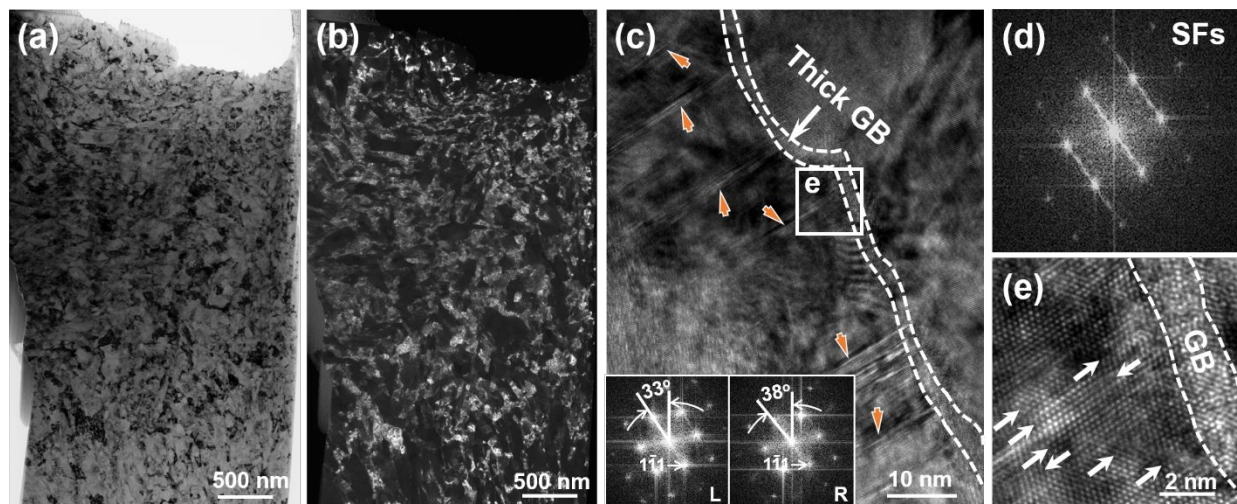


Figure 4. (a) BF and (b) DF TEM image of the deformed pillar from the heat-treated specimen after 36% of compression strain. (c) HRTEM image of grains after compression showing high density SFs (as indicated by orange arrows). These SFs were blocked by a thick GB. (d) The SFs

are verified by the corresponding FFT pattern. (e) The HRTEM image of the white box e in Fig.4c showing the blocking of SFs (indicated by white arrows) by the thick GB.

Most prior studies focused on the formation mechanism of GB complexion after heat treatment ^{52,70}. However, the influence of GB complexion on the mechanical properties of metallic materials is less well understood. Khalajhedayati *et al* ^{32,34} systematically investigated the formation of GB complexions in nanocrystalline Cu-Zr alloys and the corresponding response of mechanical properties. Their study reveals that AIFs form after heat treatment above 850 °C and the Cu-Zr alloy with amorphous interfaces exhibits a yield strength exceeding 1 GPa and a strain to failure of more than 50%. The extraordinary mechanical properties are attributed to two factors: the crystalline/amorphous interface that impacts the nucleation and transmission of dislocations, and the reduced boundary energy resulting from GB segregation ^{32,34}. Vo *et al* ^{53,54} also attributed the strengthening of nanocrystalline Cu-Nb, Cu-Fe and Cu-Ag alloys with GB segregations to the reduced GB energy comparing with the pure Cu. Both MD simulations and experimental results reveal that the strength increases monotonically with reduction of GB energy ^{32,34,53}. It was argued that reducing GB energy may make the nucleation and propagation of dislocation harder during deformation ³⁴. Rupert *et al* ⁷¹ also attributed the strengthening to the reduction in the number of available sources for dislocation emission. Both experiments and MD simulations have suggested that the solute segregation to GBs can reduce GB energy. By ignoring the entropy change of the system on adding solutes to GBs, the GB energy (γ) can be calculated by ^{54,72,73}:

$$\gamma = \gamma_0 - \Gamma \Delta H_{seg} \quad (4),$$

where γ_0 is GB energy of undoped state, Γ represents average coverage of solute in the GB (proportional to solute concentration) and ΔH_{seg} is the enthalpy of segregation. As ΔH_{seg} is positive for Ni-Mo system, the segregation of Mo in GB is beneficial for the reduction of GB energy, leading to the formation of thick GB. The underlying strengthening mechanism due to thick GBs will be discussed in detail based on MD simulation results presented in the following section.

4.3 Strengthening mechanisms revealed by MD simulations

Foregoing discussions confirm that thick GBs are indeed strong barriers to the transmission of dislocations. The fundamental mechanisms behind thick GB induced strengthening, however, remain largely unclear. In what follows, we discuss the strengthening mechanisms revealed by MD simulations.

MD simulations were performed on model NiMo alloys containing a thin (conventional) $\Sigma 5$ GB (2-3 atomic layers) and a 2.5 nm thick amorphous boundary (mimicking the experimental observation of amorphous like disordered thick GBs). The stress strain response in Fig. 5a reveals that the sample with thin GBs yields at ~ 2.9 GPa, whereas the yielding of the thick GB specimen occurs at higher stress, ~ 3.5 GPa, consistent with the experimental studies. The magnified stress-strain curves in Fig.5b show a couple of labels at various strain levels, and the microstructure evolution at positions will be shown next.

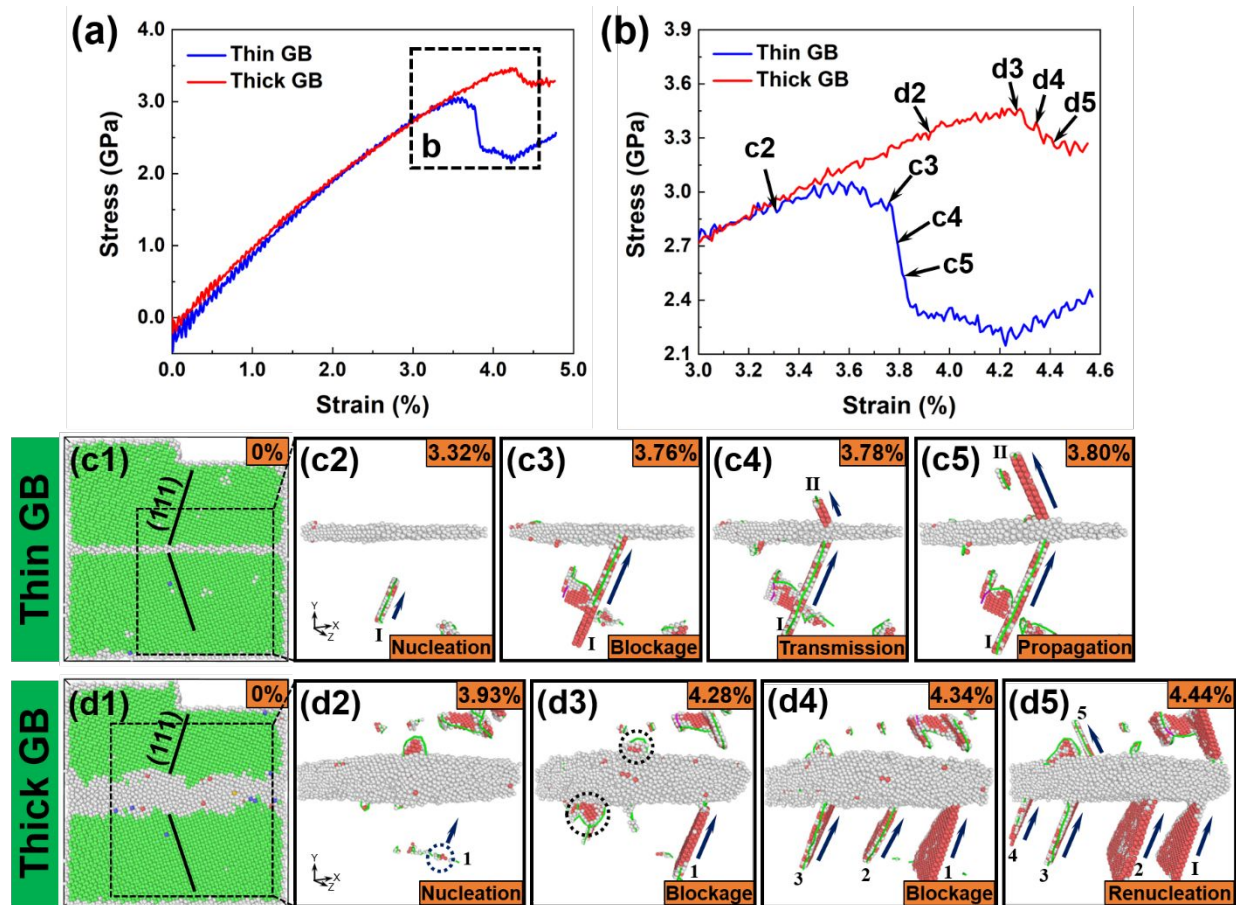


Figure 5. MD simulations of NiMo alloy with thin and thick GB. (a) The comparison of stress-strain curves for NiMo alloy with thin and thick GB under tension. The yield stress of the thin GB sample is ~ 2.9 GPa, whereas that of thick GB sample reaches ~ 3.5 GPa. (b) The magnified stress-strain curves showing the yielding behaviors of thin and thick GB samples. Evolution of atomistic configurations of (c) thin GB and (d) thick GB samples at different strains illustrated in Ovito using common neighbor analysis. FCC atoms are colored in green, HCP atoms are colored in red and amorphous atoms are colored in gray. Using dislocation analysis, the green and purple lines represent Shockley partials and stair-rod dislocations, respectively. See supplementary video 3 and 4 for more details.

The evolution of atomistic configurations for both samples under tension with increasing of strain are illustrated in Ovito using common neighbor analysis and represented in Fig.5c and 5d, respectively. FCC, HCP and amorphous atoms are colored in green, red and gray, respectively. The (111) planes of lower and upper grain forming $\Sigma 5$ grain relationship in simulation cell are labeled in Fig.5c1 and 5d1. The detailed microstructure evolutions in the dashed boxes in Fig.5c1 and 5d1 are shown in Fig.5c2-5c5 and Fig.5d2-5d5. Using dislocation analysis, the green and purple lines represent Shockley partials and stair-rod dislocations, respectively. FCC atoms were removed for clarification. For thin GB sample, Shockley partials nucleated and thereafter disappeared frequently under tension to accommodate the strain. The first set of stable Shockley partials was captured until the strain increased to $\sim 3.32\%$, as shown in Fig.5c2. The stable Shockley partials propagated towards and then blocked by the thin GB when strain increased to $\sim 3.76\%$, as illustrated in Fig.5c3. A further increase of the strain resulted in the transmission (in Fig.5c4) and further propagation (in Fig.5c5) of Shockley partials through the thin GB, contributing to the drastic stress drop as shown in Fig.5b. The snapshot reveals that the Shockley partials transmitted through the thin GB follow the $\Sigma 5$ twinning orientation relationship. Similar transmission phenomena have been reported in other MD simulation studies as well ^{74,75}.

For the thick GB sample, the dislocation activity before yielding is similar with the thin GB sample. The difference is that the first set of stable Shockley partials wasn't captured until the strain increased to $\sim 3.93\%$, as shown in Fig.5d2, higher than that (3.32%) of thin GB sample. The Shockley partial then propagated towards the thick GB and was blocked. When the tensile strain increases to $\sim 4.28\%$, plastic yielding took place, as shown in Fig.5d3. Comparing to the Shockley partial transmission induced yielding for thin GB sample, the yielding of thick GB

sample was attributed to the nucleation and propagation of more Shockley partials in the lower grain, as shown in Fig.5d4. At this stage, several pre-existing Shockley partials nucleated before yielding (as labeled by black dotted circles in Fig.5d3) disappeared, presumably due to their absorption by the thick GB. With the further increase of the strain, a new Shockley partial (labeled as #V) nucleated and propagated above the thick GB at the strain of ~4.44% (as illustrated in Fig.5d5), leading to the further stress decrease. It is worth mentioning that the new Shockley partial (V) in the upper grain did not occur at the coincident site where the Shockley partials (I-IV) intercept with the thick GB. The comparison of the evolution of new activated Shockley partials in the upper grain for both samples are presented in Suppl. Fig.4. It shows two Shockley partials have transmitted cross the thin GB (at the same incident sites) after yielding and propagated upwards, as illustrated by the black arrows in Suppl. Fig.4a. In contrast, Shockley partials (I-IV) once blocked by the thick GBs, often propagated along directions parallel to the GB, as denoted by arrows in Suppl. Fig.4b. These evidences suggest that the deformation mechanisms of thin GB and thick GB samples are different. Transmission of Shockley partials across the thin GB attributes to the yielding of the thin GB sample. For thick GB sample with amorphous boundary, however, no apparent transmission phenomenon has been observed during deformation. And the plastic yielding is derived from the renucleation of new Shockley partials on either side of thick GBs. See Supplementary video 3 and 4 for more details.

Previous studies on Cu/amorphous CuZr multilayers show that during deformation, the glide dislocations nucleated in Cu layer were absorbed by the crystalline/amorphous interface, and alleviate the atomic shear strain concentration on amorphous layer^{76,77}. These observations

imply that the interface between crystalline and disordered structure could be an effective dislocation sink during deformation. Upon absorption by the interface, the dislocation core will dissociate or spread, and thus the stress/strain concentration at the interface will be smeared. Consequently, the singularity that enables the dislocation to slip through lattice is lost, and a higher stress is necessary to promote the transmission of dislocations across the interface, resulting in higher yield stress. MD simulations on Cu/Nb multilayers with FCC/BCC structure also reveal that a single dislocation cannot slip through the Cu/Nb layer interface even at a resolved shear stress of 1.0 GPa²⁰. In this study, the strengthening from the thick disordered GBs may also arise from the absorption of dislocations by the GBs. To verify our hypothesis, the evolution of total length of Shockley partials of both samples with increasing strain has been statistically calculated and plotted in Fig.6a. It shows that the length of Shockley partials (dislocation density) for thin GB sample increased drastically after straining beyond ~3.0%. The total length increased from ~400 nm to over 1100 nm after yielding, resulting from the transmission and propagation of Shockley partials through the thin GB. In comparison, for the thick GB specimen, the total length of Shockley partials didn't increase until being strained to ~3.3%, and the corresponding increase of dislocation length is much less than the thin GB sample. Fig.6b reveals that the partials have indeed been absorbed by the thick GB during deformation. The absorption of partials smeared the stress/strain concentration at the boundary and prevented the transmission of Shockley partials from happening. Consequently, the yielding of thick GB sample takes place at higher strain and stress level compared with the thin GB sample.

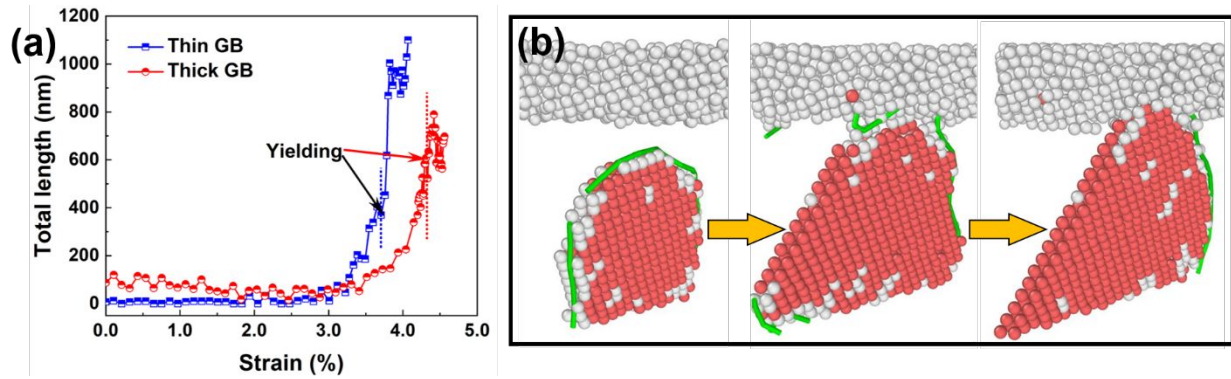


Figure 6. (a) The evolution of total length of Shockley partials for thin and thick GB samples with increasing of strain. The total length of Shockley partials is much greater for the thin GB specimen and increases sharply after yielding. (b) Evolution of atomistic configurations showing the absorption of Shockley partials by the amorphous thick GB.

5. Conclusion

In summary, we reported the formation of ~ 3 nm thick GBs in nanocrystalline NiCrMo alloy after heat treatment. The Ni alloy with thick GBs is much stronger than the nanocrystalline Ni alloys with conventional (thin) GBs. The thick GBs effectively block the transmission of dislocations by acting as dislocation sinks, as confirmed by explicit MD simulations. This study provides new perspective for the design of high-strength, deformable nanocrystalline metals.

Acknowledgements

J. Ding and X. Zhang acknowledge primary financial support by DOE-Nuclear Energy under DE-NE0008549. S. Xue and H. Wang acknowledge financial support by ONR Office of Naval Research N00014-17-1-2087 (sample preparation and in situ SEM), and N0014-16-1-2778 (for TEM work). Q. Li. is supported by Department of Energy - BES (Grant No. DE-SC0016337) on performing micropillar preparation experiments. We acknowledge Prof. Alejandro Strachan and Dr. Guda Vishnu Karthik from School of Materials Engineering in Purdue University for useful discussion. Accesses to microscopy facilities at Life Science and School of Materials Engineering at Purdue University and Center for Integrated Nanotechnologies at Los Alamos National Laboratory are also acknowledged.

Reference

- 1 E. O. Hall, *Proc. Phys. Soc. London Sect. B*, 1951, **64**, 747–753.
- 2 J. Gil Sevillano, P. van Houtte and E. Aernoudt, *Prog. Mater. Sci.*, 1980, **25**, 69–134.
- 3 N. Hansen, *Scr. Mater.*, 2004, **51**, 801–806.
- 4 Y. M. Wang, E. Ma and M. W. Chen, *Appl. Phys. Lett.*, 2008, **80**, 2395-2397.
- 5 R. Valiev, *Nat. Mater.*, 2004, **3**, 511–516.
- 6 T. G. Nieh and J. Wadsworth, *Scr. Metall. Mater.*, 1991, **25**, 955–958.
- 7 N. Y. C. Yang, T. J. Headley, J. J. Kelly and J. M. Hruby, *Scr. Mater.*, 2004, **51**, 761–766.
- 8 J. Hu, Y. N. Shi, X. Sauvage, G. Sha and K. Lu, *Science*, 2017, **355**, 1292–1296.
- 9 K. S. Kumar, S. Suresh, M. F. Chisholm, J. A. Horton and P. Wang, *Acta Mater.*, 2003, **51**, 387–405.

- 10 Y. F. Zhang, S. Xue, Q. Li, C. Fan, R. Su, J. Ding, H. Wang, H. Wang and X. Zhang, *Scr. Mater.*, 2018, **148**, 5–9.
- 11 Q. Li, S. Xue, J. Wang, S. Shao, A. H. Kwong, A. Giwa, Z. Fan, Y. Liu, Z. Qi, J. Ding, H. Wang, J. R. Greer, H. Wang and X. Zhang, *Adv. Mater.*, 2018, **30**, 1704629.
- 12 M. Callisti and T. Polcar, *Acta Mater.*, 2017, **124**, 247–260.
- 13 J. Li, Y. Chen, S. Xue, H. Wang and X. Zhang, *Acta Mater.*, 2016, **114**, 154–163.
- 14 K. Y. Yu, Y. Liu, S. Rios, H. Wang and X. Zhang, *Surf. Coatings Technol.*, 2013, **237**, 269–275.
- 15 Y. Chen, Y. Liu, C. Sun, K. Y. Yu, M. Song, H. Wang and X. Zhang, *Acta Mater.*, 2012, **60**, 6312–6321.
- 16 X. Zhang, A. Misra, H. Wang, T. D. Shen, M. Nastasi, T.E. Mitchell, J. P. Hirth, R. G. Hoagland and J. D. Embury, *Acta Mater.*, 2004, **52**, 995–1002.
- 17 Y. Liu, D. Bufford, H. Wang, C. Sun and X. Zhang, *Acta Mater.*, 2011, **59**, 1924–1933.
- 18 M. D. Sangid, T. Ezaz, H. Sehitoglu and I. M. Robertson, *Acta Mater.*, 2011, **59**, 283–296.
- 19 M. De Koning, R. Miller, V. V Bulatov and F. F. Abraham, *Philos. Mag. A*, 2002, **82**, 2511–2527.
- 20 J. Wang, R. G. Hoagland, J. P. Hirth and A. Misra, *Acta Mater.*, 2008, **56**, 5685–5693.
- 21 R. G. Hoagland, R. J. Kurtz and C. H. Henager, *Scr. Mater.*, 2004, **50**, 775–779.
- 22 B. Ham and X. Zhang, *Mater. Sci. Eng. A*, 2011, **528**, 2028–2033.
- 23 Z. Fan, S. Xue, J. Wang, K. Y. Yu, H. Wang and X. Zhang, *Acta Mater.*, 2016, **120**, 327–336.

- 24 V. Gavriljuk, H. Berns, C. Escher, N. Glavatskaya, A. Sozinov and Y. Petrov, *Mater. Sci. Eng. A*, 1999, **271**, 14–21.
- 25 W. Sigle, G. Richter, M. Rühle and S. Schmidt, *Appl. Phys. Lett.*, 2006, **89**, 1–4.
- 26 V. K. Gupta, D. H. Yoon, H. M. Meyer and J. Luo, *Acta Mater.*, 2007, **55**, 3131–3142.
- 27 X. Shi and J. Luo, *Appl. Phys. Lett.*, 2009, **94**, 11–13.
- 28 J. Luo, H. K. Cheng, K. M. Asl, C. J. Kiely and M. P. Harmer, *Science*, 2011, **333**, 1730–1734.
- 29 A. Kundu, K. M. Asl, J. Luo and M.P. Harmer, *Scr. Mater.*, 2013, **68**, 146–149.
- 30 P. R. Cantwell, M. Tang, S. J. Dillon, J. Luo, G. S. Rohrer and M. P. Harmer, *Acta Mater.*, 2013, **62**, 1–48.
- 31 T. Frolov, *Appl. Phys. Lett.*, 2014, **104**, 1–4.
- 32 A. Khalajhedayati and T. J. Rupert, *Jom*, 2015, **67**, 2788–2801.
- 33 S. J. Dillon, K. Tai and S. Chen, *Curr. Opin. Solid State Mater. Sci.*, 2016, **20**, 324–335.
- 34 A. Khalajhedayati, Z. Pan and T. J. Rupert, *Nat. Commun.*, 2016, **7**, 1–8.
- 35 D.R. Clarke and G. Thomas, *J. Am. Ceram. Soc.*, 1977, **60**, 491–495.
- 36 J. Ding, Q. Li, J. Li, S. Xue, Z. Fan, H. Wang and X. Zhang, *Acta Mater.*, 2018, **149**, 57–67.
- 37 I. N. Sneddon, *Int. J. Eng. Sci.*, 1965, **3**, 47–57.
- 38 S. Plimpton, *J. Comput. Phys.*, 1995, **117**, 1–19.
- 39 A. Stukowski, *Model. Simul. Mater. Sci. Eng.*, 2010, **18**, 015012.

- 40 A. Stukowski, V. V. Bulatov and A. Arsenlis, *Model. Simul. Mater. Sci. Eng.*, 2012, **20**, 085007.
- 41 Z. Pan and T. J. Rupert, *Acta Mater.*, 2015, **89**, 205–214.
- 42 X. W. Zhou, R. A. Johnson and H. N. G. Wadley, *Phys. Rev. B*, 2004, **69**, 144113.
- 43 G. D. Hughes, S. D. Smith, C. S. Pande, H. R. Johnson and R. W. Armstrong, *Scr. Metall.*, 1986, **20**, 93–97.
- 44 N. Wang, Z. Wang, K. Aust and U. Erb, *Mater. Sci. Eng. A*, 1997, **237**, 150–158.
- 45 F. Ebrahimi, G. Bourne, M. Kelly and T. Matthews, *Nanostructured Mater.*, 1999, **11**, 343–350.
- 46 C. Xiao, R. A. Mirshams, S. H. Whang and W. M. Yin, *Mater. Sci. Eng. A*, 2001, **301**, 35–43.
- 47 F. Dalla Torre, H. Van Swygenhoven and M. Victoria, *Acta Mater.*, 2002, **50**, 3957–3970.
- 48 C. A. Schuh, T. G. Nieh and T. Yamasaki, *Scr. Mater.*, 2002, **46**, 735–740.
- 49 K. S. Raju, M. G. Krishna, K. A. Padmanabhan, K. Muraleedharan, N. P. Gurao and G. Wilde, *Mater. Sci. Eng. A*, 2008, **491**, 1–7.
- 50 N. Krasilnikov, W. Lojkowski, Z. Pakiela and R. Valiev, *Mater. Sci. Eng. A*, 2005, **397**, 330–337.
- 51 A. P. Zhilyaev, A. A. Gimazov, E. P. Soshnikova, Á. Révész and T. G. Langdon, *Mater. Sci. Eng. A*, 2008, **489**, 207–212.
- 52 J. D. Schuler and T. J. Rupert, *Acta Mater.*, 2017, **140**, 196–205.

- 53 S. Özerinç, K. Tai, N. Q. Vo, P. Bellon, R. S. Averback and W. P. King, *Scr. Mater.*, 2012, **67**, 720-723.
- 54 N. Q. Vo, J. Schäfer, R. S. Averback, K. Albe, Y. Ashkenazy and P. Bellon, *Scr. Mater.*, 2011, **65**, 660-663.
- 55 M. Herbig, M. Kuzmina, C. Haase, R. K. W. Marceau, I. Gutierrez-Urrutia, D. Haley, D. A. Molodov, P. Choi and D. Raabe, *Acta Mater.*, 2015, **83**, 37-47.
- 56 S. J. Dillon, M. Tang, W. C. Carter and M. P. Harmer, *Acta Mater.*, 2007, **55**, 6208-6218.
- 57 C. W. Corti, *Platin. Met. Rev.*, 1986, **30**, 184–195.
- 58 H. T. Wang, N. R. Tao and K. Lu, *Scr. Mater.*, 2013, **68**, 22–27.
- 59 Y. Samih, B. Beausir, B. Bolle and T. Grosdidier, *Mater. Charact.*, 2013, **83**, 129–138.
- 60 R. Huang and Y. Han, *J. Alloys Compd.*, 2013, **554**, 1–11.
- 61 T. Zhu and J. Li, *Prog. Mater. Sci.*, 2010, **55**, 710–757.
- 62 X. H. Chen, J. Lu, L. Lu and K. Lu, *Scr. Mater.*, 2005, **52**, 1039–1044.
- 63 L. Lu, M. L. Sui and K. Lu, *Science*, 2000, **287**, 1463–1466.
- 64 R. Pippan, S. Scheriau, A. Taylor, M. Hafok, A. Hohenwarter and A. Bachmaier, *Annu. Rev. Mater. Res.*, 2010, **40**, 319–343.
- 65 N. Tsuji, Y. Saito, S. H. Lee and Y. Minamino, *Adv. Eng. Mater.*, 2003, **5**, 338–344.
- 66 T. Chookajorn, H. A. Murdoch and C. A. Schuh, *Science*, 2012, **337**, 951-954.
- 67 T. J. Rupert, *Scr. Mater.*, 2014, **81**, 44–47.

- 68 C. A. Schuh, T. G. Nieh and H. Iwasaki, *Acta Mater.*, 2003, **51**, 431–443.
- 69 A. Misra, J. P. Hirth and R. G. Hoagland, *Acta Mater.*, 2005, **53**, 4817–4824.
- 70 F. Abdeljawad, P. Lu, N. Argibay, B. G. Clark, B. L. Boyce and S. M. Foiles, *Acta Mater.*, 2017, **126**, 528-539.
- 71 T. J. Rupert, J. R. Trelewicz, C. A. Schuh, *J. Mater. Res.*, 2012, **27**, 1285-1294.
- 72 J. Weissmüller, *Nanostructured Mater.*, 1993, **3**, 261-272.
- 73 J. Weissmüller, *J. Mater. Res.*, 1994, **9**, 4–7.
- 74 X. Zhang, A. Misra, H. Wang, M. Nastasi, J. D. Embury, T. E. Mitchell, R. G. Hoagland and J. P. Hirth, *Appl. Phys. Lett.*, 2004, **84**, 1096–1098.
- 75 X. Zhang, A. Misra, H. Wang, A. L. Lima, M. F. Hundley and R. G. Hoagland, *J. Appl. Mech.*, 2005, **97**, 094302.
- 76 Y. Cui, O. T. Abad, F. Wang, P. Huang, T. J. Lu, K. W. Xu and J. Wang, *Sci. Rep.*, 2016, **6**, 2–7.
- 77 Y. Cui, Y. Shibutani, S. Li, P. Huang and F. Wang, *J. Alloys Compd.*, 2017, **693**, 285–290.